Field dependent electrical and thermal transport in polycrystalline WSe_2

W. Y. Kim,[1,2] H. J. Kim,[1,2] Toby Hallam,[2,3] Niall McEvoy,[2] Riley Gatensby,[2] H. Nerl,[2] K. O'Neill,[2] R. Siris,[4] G.-T. Kim,[1] and Georg S. Duesberg[2,4 a)]

[1]School of Electrical Engineering, Korea University, Seoul 136-701, South Korea
[2]CRANN, AMBER and School of Chemistry, Trinity College Dublin, Dublin 2, Ireland
[3]School of Electrical and Electronic Engineering, Newcastle University, Newcastle-upon-Tyne, United Kingdom
[4]Institute of Physics, EIT 2, Faculty of Electrical Engineering and Information Technology, Universität der Bundeswehr, München, Germany
E-mail: duesberg@unibw.de

Keywords: 2D materials, transition metal dichalcogenide, thermoelectrics, field effect transistor

Abstract

Owing to their desirable electrical and thermoelectric properties, transition metal dichalcogenides (TMDs) have attracted significant attention in recent years. Therefore, it is important to develop reliable synthetic methods and device fabrication processes for TMDs. In this study, WSe_2 films were synthesized on a large scale by thermally assisted conversion (TAC) of W films on SiO_2/Si substrates at 600°C. The TAC process yields homogeneous polycrystalline films of controlled thickness over large areas which have the advantage that they can be adapted for mass production for multiple applications. In this regard, pre-patterning of the deposited metal films allows for devices to be easily fabricated without any etch process. UV-lithography-defined W structures have been deposited and after conversion to WSe_2 their electrical and thermoelectric properties have been studied. Using e-beam lithography, a field effect transistor (FET) with a WSe_2 channel was fabricated. It showed p-type behavior and reasonable field effect mobility of ~1 $cm^2 \cdot V^{-1} \cdot s^{-1}$. The thermoelectric properties were analyzed by integrating a micro-heater in vicinity to the WSe_2 FET. The maximum Seebeck coefficient and power factor ($S^2 \cdot \sigma$) values were calculated to be ~61 $\mu V \cdot K^{-1}$ (V_g = 45 V) and ~1.3 $nW \cdot K^{-2} \cdot cm^{-1}$, respectively.

1. Introduction

Transition metal dichalcogenides (TMDs) have attracted tremendous attention as next-generation semiconductor nanomaterials. Unlike graphene, a number of two-dimensional (2D) TMDs have an intrinsic bandgap and exhibit fascinating electrical and optical properties.[1-4] TMDs have a layered structure in which the transition metal forms a hexagonal layer which is sandwiched between two hexagonal layers of the chalcogen. The TMD monolayers are bonded to each other by weak van der Waals forces, and thus can be considered a 2D material. A number of studies have shown the various applications of TMDs as sensors and in electronic, photonic, and optoelectronic devices.[2,5,6] Another field of critical importance is energy harvesting with thermoelectric power which has gained rapid momentum due to the discovery of various nanomaterials. [7-19] Recently, large thermopower values and efficiencies have been demonstrated in TMDs.[20-23]. Thus, TMDs have great potential as thermoelectric materials, however most studies have been carried out on mechanically exfoliated TMD monolayers, where it is not possible to control the size and geometry of the device.

In order to utilize the high efficiencies and the small device volume of 2D materials for thermoelectric applications, it is an absolute pre-requisite to develop a system for homogeneous, large-scale synthesis of TMDs. Thus, the large-scale synthesis of TMDs and device fabrication using such large-scale grown TMD films has become a prominent research area for future semiconductor applications. Recently, TMD films have been synthesized on a large scale by film growth techniques such as chemical vapor deposition (CVD) and thermally assisted conversion (TAC) of the pre-deposited metal films.[23-31] While CVD produces well-defined monolayers, it struggles to produce continuous films. TAC on the other hand produces continuous films of controlled thickness with a polycrystalline morphology.[29,32]

Tungsten diselenide (WSe_2) is one of the most studied TMDs after molybdenum disulfide (MoS_2). Several studies of WSe_2 have discussed its excellent electrical and thermoelectric properties.[4,22,33-36] The power factor ($S^2\sigma$) of WSe_2 (~40 $\mu WK^{-2}cm^{-1}$)[22] is comparable with

the value of TiS_2 (37 $\mu WK^{-2}cm^{-1}$)[37], which is one of the best performing thermoelectric 2D materials. In addition, recently ultralow thermal conductivity in WSe_2 was demonstrated.[38] Thus, a more competitive figure of merit ($ZT = S^2 \cdot \sigma \cdot T/\kappa$) can be expected for WSe_2.

In this study, WSe_2 films were synthesized on a large scale by TAC on a SiO_2/Si substrate. The growth of the films takes place at a temperature of 600 °C, which is very low compared to that required for CVD synthesis, and beneficial for device fabrication. The TAC process yields homogeneous polycrystalline films of controlled thickness over large areas. Pre-patterning of the deposited metal films allows for devices to be easily fabricated without any etch process. In this work, UV-lithography-defined W structures were deposited on the substrate and subsequently converted to WSe_2. Using e-beam lithography, we were able to apply metal electrode contacts and heating elements onto the WSe_2 channels yielding field effect transistor (FET) type devices which allowed the gate-dependent electrical and thermoelectric transport properties of polycrystalline WSe_2 to be determined.

2. Results and discussion

2.1. Synthesis and Characterization

Thin W films deposited on the SiO_2/Si substrates are converted in selenium vapor at 600 °C to WSe_2, as shown schematically in Figure 1(a). This method was previously described for MoS_2 and $MoSe_2$ thin films.[29,32] The WSe_2 films were synthesized at a lower temperature than previously reported for this material.[22,27] This relatively low temperature can reduce damage to the substrates during synthesis.[39] The thickness of converted WSe_2 film can be controlled by changing the thickness of pre-deposited W. Selected-area deposition of the W prior to TAC also allows the definition of WSe_2 patterns without an etch process. Apart from simplicity, the absence of an etch process is also important because the 2D materials can be easily damaged and contaminated during either wet or dry etch process. The TAC process is

free from the above-mentioned damage and contamination problems and the entire device fabrication process is fully controlled.

In this study, various thicknesses of W film were deposited and the TAC processes were then performed. Though there is a slight performance difference depending on the thickness, p-type behavior was confirmed over all samples. (Figure S4) It is observed that the thermoelectric power increases as the thickness of WSe_2 decreases. (Figure S5) The detailed electrical and thermoelectric characterization were conducted focusing on the 7.5 nm W sample because this sample has the middle range of the W thicknesses used in the experiments, and shows the most stable performance on repeated measurements.

Figure 1(c) and (d) show an optical microscope image of a predefined W film and converted WSe_2 film. The light green square regions indicate the prestructured W and WSe_2 film which was patterned by optical lithography. Figure 1(e) and (f) show an atomic force microscopy (AFM) image of the W and WSe_2 film. It can be seen that the surface of WSe_2 film is smooth apart from some agglomerated WSe_2 particles which formed during synthesis. By taking the AFM line profiles (shown as the inset of Figure 1(e) and (f)), it was observed that the thickness of the film changed from ~7.5 nm for the predeposited W film to ~ 13.7 nm after conversion. (each thickness value is a mean value from several points) This is due to the incorporation of the Se into the pristine metal film and is commensurate with previous reports describing the process.[29] The empirical atomic radius of W is 0.14 nm, and covalent radius is ~0.17 nm.[40,41] In WSe_2, the length of W-Se and Se-Se bonds are 0.25 and 0.33 nm, respectively.[42] The thickness of monolayer WSe_2 is ~0.65 nm. Since the W film deposited by sputtering has an incomplete crystal structure compare to the bulk single crystal (body centered cubic), the deposited W film has larger volume than bulk. Also it could be partly oxidized during or after sputtering. Thus, the volume (thickness) change from W (~7.5 nm) to TAC-grown WSe_2 (~13.7 nm) is reasonable. Also it is possible that some W was removed during the relatively long conversion process. A Raman spectrum of the WSe_2 film is shown

in Figure 1(b). One significant peak can be observed at ~250 cm^{-1}, which corresponds to the overlap of the E^1_{2g}, A_{1g} and 2LA(M) Raman-active modes of WSe_2.[43] The presence of these peaks confirms that the W film was successfully converted to WSe_2.[43,44] Further Raman spectra of TAC-grown WSe_2 films of varying growth temperatures and times are presented in supporting information. (Figure S3)

2.2. Electrical properties

A device consisting of four Ti/Au electrodes separated by a distance of 1, 3, or 10 μm on an 80 μm wide WSe_2 channel for electrical measurements was fabricated by using e-beam lithography. Figure 2(a) shows the schematic image of the WSe_2 device and the inset of Figure 2(b) shows the optical microscope image of this device. Initially, the electrical properties of WSe_2 were measured at room temperature under ambient conditions using the highly-doped Si substrate as a back gate for field-effect transport measurements. Figure 2(b) shows the transfer characteristics of the TAC-grown WSe_2 device at V_{ds} = 10 mV. Gate bias was applied in the ±60 V range. Figure 2(c) shows the output characteristics of the WSe_2 films. It was confirmed from the linear shape of the I–V curves that the metal-semiconductor contact barrier does not affect the device properties. The WSe_2 film showed p-type conduction, in agreement with theory. The maximum field effect mobility is 0.911 $cm^2 V^{-1}\cdot s^{-1}$, determined by using the equation

$$\mu_{FE} = g_m \frac{L}{WC_{ox}V_{ds}}, \qquad \textbf{Equation (1)}$$

where L = 3 μm, $g_m = dI_{ds}/dV_{gs}$ is the transconductance and $C_{ox} = \varepsilon_0\varepsilon_r/t$ (ε_r = 3.9, t = 300 nm) is the oxide capacitance between the channel and the back gate per unit area. This value is reasonably high considering that a large-scale fabricated channel of polycrystalline WSe_2 on SiO_2 was investigated. Other reports of helium-ion beam damaged crystalline WSe_2 have reported values of 2–64 $cm^2\cdot V^{-1}\cdot s^{-1}$, which is in the same range [45] A slight hysteresis is seen in the transfer curve, which is attributed to the fact that the electrical measurements were

carried out under ambient conditions, meaning the surface of the WSe_2 channel could be affected by O_2 or H_2O molecules in the air.

A high conductivity of ~45 $S \cdot m^{-1}$ in the on state of the device, and also a high off-state current (~70 nA) is observed giving a value of 2.2 for the on/off ratio. This low value is attributed to the polycrystalline structure of the TAC-grown TMD films which consist of domains of tens of nanometer in size. [28,31,32] Therefore, a lot of defects exist between domain boundaries. It is likely that these defects are electrically active as dopants, resulting in a high off-state current.[46,47] Such a high defect density also reduces the ability of the gate to modulate current, which leads to depressed mobility.

2.3. Thermoelectric power properties

For thermoelectric power (TEP) measurement of the TAC grown WSe_2 films, a microscale thermoelectric device was fabricated by using electron beam lithography, and a microheater and microthermometers were also included in the device. Figures 3(a) and 3(b) show the schematics of the WSe_2 microscale device used for TEP measurements and its optical microscope image, respectively. This type of device structure has been previously used for thermoelectric measurements of other microscale materials.[8,9,12,13,17,18,21,22] The electrode for the microheater was fabricated close to WSe_2 films, and a temperature gradient (ΔT) was induced by Joule heating when voltage (V_{heat}) was applied. Two four-probe measurement electrodes (TM_{top} and TM_{bot}) were also fabricated on the WSe_2 film. The thermovoltage (ΔV_{TE}) across the device could be measured by using these electrodes. These electrodes also functioned as on-chip microthermometers as the resistance of a metal increased with increasing temperature. The applied V_{heat} was varied from 0 to 3 V and the relationship between the thermoelectric voltage (ΔV_{TE}) and V_{heat}^2 determined by this experiment is illustrated in Figure 3(c). The minimum and maximum bars show the range of the measured values, and the standard error represented as a box. As Joule heating is proportional to

V_{heat}^2/R, ΔV_{TE} is found to be proportional to V_{heat}^2. The sign of the thermovoltage is negative (as shown in Figure 3(c)), which means that holes are the majority charge carriers. This is in agreement with the p-type conduction behavior of the TAC-grown WSe_2 films that was revealed in the previous FET measurements. The maximum thermovoltage (mean value) is −46.3 μV at V_{heat} = 3 V (V_g = 0 V induced). The relationship between the temperature gradient (ΔT) and V_{heat}^2 is shown in Figure 3(d) with the minimum and maximum values represented as a bar and the standard deviation is indicated with a box. The changes in the resistance of TM_{bot} and TM_{top} electrodes were measured at various induced heat voltages (V_{heat}) by four-probe measurement (Figure S4), and the ΔT of each electrode was calculated from the values of measured resistance by using the relation $R = R_0[1 + \alpha(T-T_0)]$, where α is the temperature coefficient of Au and R_0 is the resistance at T_0 (initial temperature). ΔT and V_{heat}^2 also have a linear relationship and the temperature of the TM_{top} electrode increases faster than that of the TM_{bot} electrode because the distance between the former and the heater electrode is smaller. Thus, ΔT of the thermoelectric device can be calculated by subtracting the ΔT of TM_{bot} from the ΔT of TM_{top}. The maximum value of ΔT obtained was 0.91 K at V_{heat} = 3 V. The relationship between ΔV_{TE} and ΔT is shown in Figure 3(e) with min, max bars and standard error box. From Figures 3(c) and 3(d), respectively, the values of ΔV_{TE} and ΔT which were obtained at the same V_{heat} were plotted. A linear relationship was shown between ΔV_{TE} and ΔT. The Seebeck coefficient can be obtained by extracting the slope of the linear fit of Figure 3(e) by using the relation $S = -\Delta V_{TE}/\Delta T$. The Seebeck coefficient of the TAC-grown WSe_2 film was thus determined to be 48 μV K^{-1}. This value is about 5 times lower than the previously reported Seebeck coefficient values of WSe_2 of mechanically-exfoliated or CVD-grown flakes. [22,23] This is attributed to the polycrystallinity and high abundance of defects in our TAC-grown materials. However, it has to be emphasized that in apposition to these materials, TAC features were produced with full control over the shape and thickness, while exfoliated and CVD-grown flakes are limited to a few micrometers in

lateral dimensions and mono to few layers in vertical size. Our TAC-grown WSe_2 compares well with other low dimensional materials such as MoS_2,[48] Bi_2Se_3,[14] Bi_2Te_3,[7] graphene,[15,16,19] carbon nanotubes,[8-10] and Si and [11] Bi nanowires.[18] However, again one most emphasize that all these materials are bottom-up grown with unresolved challenges in fabrication of TEP devices, while TAC films are compatible with large-scale, top-down structuring methods.

For a more detailed analysis, measurements of the thermoelectric power as dependent on the gate voltage applied to the substrate were performed. The gate-voltage dependence of electrical conductivity and Seebeck coefficient was determined under ambient conditions and at room temperature, and the results are shown in Figure 4(a). For obtaining accurate conductivity values, the contact resistance (R_c) of the thermoelectric device was extracted by using the transmission line method (TLM). (Figure S6) The extracted R_c is ~57 kΩ. Electrical conductivity (red, right *y* axis) shows a p-type behavior which increases when the gate bias increases to a negative value. The gate dependence of the Seebeck coefficient (blue, left *y* axis) shows a curve which is inversely proportional to the electrical conductivity curve. The relationship between electrical conductivity and Seebeck coefficient is given by the Mott relation.[49,50]

$$S = -\frac{\pi^2 {k_B}^2 T}{3|e|}\frac{1}{\sigma}\frac{d\sigma}{dE}\bigg|_{E_f}, \qquad \textbf{Equation (2)}$$

where k_B is the Boltzmann constant and E_f is the Fermi level of the sample. Given that we are dealing with a polycrystalline film, the amount of resistance change is different for each WSe_2 crystal as V_g changes. Because of this difference, when V_g increases there are some regions where the resistance decreases to a larger extent compared to other regions. However, the resistance of the entire film does not change much because most of the current flows through the low resistance path. On the contrary, the locally increased thermoelectric power from the crystals with reduced resistance increases the thermoelectric power of the entire device.

Therefore, a drastic change of the Seebeck coefficient value is observed compared to the conductivity change. The thermoelectric power factor ($S^2 \cdot \sigma$) can be extracted. The gate-voltage dependence of the power factor shows a similar shape as the gate dependence of the Seebeck coefficient (Figure 4(b)). Since the variation of the Seebeck coefficient is bigger than that of the electrical conductance, the value of the Seebeck coefficient is the dominant factor to determine the power factor in our samples. The maximum power factor is close to 1.27 $nW \cdot K^{-2} \cdot cm^{-1}$. This value is considerably smaller than that of mechanically-exfoliated or CVD-grown monolayer WSe_2 flakes, because these materials have a much higher conductivity than bulk WSe_2.[22,23] The here reported over 10 nm thick TAC-grown WSe_2 has conductivities in the bulk regime. However, the power factor can be optimized by thickness control of TAC-grown WSe_2, which is the subject of current investigations. Moreover, the most precise figure of merit which determines the performance of a TEP device is $ZT = S^2 \cdot \sigma \cdot T/\kappa$, where S is the Seebeck coefficient, T is temperature, and σ and κ are electrical and thermal conductivity, respectively. The κ of polycrystalline TAC-grown WSe_2 should be smaller than that of single-crystal WSe_2, because numerous grain/domain boundaries interfere with the thermal transport. In the case of MoS_2, the κ of polycrystalline films is 10–100 times lower than single-crystal monolayers.[23,51,52] Therefore it can be expected that our TAC-grown WSe_2 will also have a much smaller κ, resulting in competitive ZT values. Thus, the measurement of thermal conductivity of TAC grown WSe_2 is imperative to evaluate the potential of this well-accessible material for TEP devices.

3. Conclusions

In this work, large-scale homogenous polycrystalline WSe_2 films were synthesized by TAC of thin W films. Furthermore, geometrically defined structures of 2D WSe_2 were fabricated with an etch-free process, by selective-area deposition of the W. By defining the contacts with e-beam lithography and using the substrate as a back gate, field effect transistors with WSe_2

channels were fabricated. These devices showed reasonable mobility values of ~1 $cm^2 \cdot V^{-1} \cdot s^{-1}$. Although a high off-state current which led to small on-off ratios was observed, this could be improved by reducing the defects present in the films. The thermoelectric properties of WSe_2 thin films were analyzed using microfabricated devices. The maximum Seebeck coefficient value was calculated to be 61 $\mu V \cdot K^{-1}$ at V_g = 45 V and the maximum power factor ($S^2 \cdot \sigma$) value was 1.27 $nW \cdot K^{-2} \cdot cm^{-1}$. The electrical and thermoelectric performances of TAC-grown WSe_2 film do not quite reach the values of other mechanically exfoliated or CVD grown TMDs or similarily derived low-dimensional materials, however they have a great advantage for large-scale fabrication and full control over the structure. Thus for circuit fabrication of next-generation electrical, optical and thermoelectric devices our TAC-grown WSe_2 films have great potential.

4. Methods

Tungsten diselenide (WSe_2) thin films were synthesized by TAC of metals following previously reported synthetic methods for MoS_2 and $PtSe_2$ thin films.[28,31] A schematic diagram of the WSe_2 film synthesis process is depicted in Figure S1. Highly doped p-type Si with a 300 nm layer of SiO_2 was used as substrate. Before the tungsten (W) metal deposition, the channel area of WSe_2 film was defined by using photolithography. W metal films were deposited onto SiO_2/Si substrates with a Gatan precision etching and sputter coating system. After lift-off, the substrates with deposited W in the selected areas were loaded into a quartz tube furnace with two heating zones. The samples were located in the second heating zone which was set to 600 °C. The temperature of the first heating zone was set at the melting point of selenium (Se, ~220 °C) and a selenium source was placed in this zone. A mixture of Ar/H_2 (9:1, 150 sccm) was used as the carrier gas to transport the vaporized Se to the W deposited samples. The carrier gas, including vaporized selenium, passed through the second heating zone and then into a cold trap. The pressure in the furnace was kept under ~0.7 torr during

selenization. A dwell-time of 2 h was employed to ensure complete selenization. Figure S1(b) shows the schematic diagram of the synthesis system for TAC.

The Raman spectra of the samples were measured using a Witec Alpha 300 R confocal Raman microscope with an excitation wavelength of 532 nm. The spectra shown for each sample were obtained by averaging ten discrete point spectra. Atomic force microscopy (AFM) measurements were carried out in a non-contact mode by using a Veeco diInnova atomic force microscope in tapping mode. Scanning electron microscopy (SEM) was carried out with a Carl Zeiss Ultra microscope.

XPS analysis was performed using a VG Scientific ESCAlab MKII system with a CLAM2 analyser and PSP twin anode, unmonochromatized Al Kα x-ray source. Spectral fitting was performed using CasaXPS software. Charge compensation used the adventitious carbon peak at 284.6~eV. A Shirley background subtraction was performed, followed by the fitting of transition metal and chalcogen doublet peaks with mixed Gaussian and Lorentzian character.

The TAC-grown selected areas of WSe_2 were contacted by e-beam lithography using the positive electron beam resist PMMA 950K A4. After a development process, four electrodes (Ti/Au – 10 nm/100 nm) with 1, 3, and 10 μm channel length were deposited using e-beam evaporation. For thermopower measurements, a heater electrode was deposited at a distance of 5 μm from the WSe_2 film and two four-probe measurement electrodes (TM_{top}, TM_{bot}) which worked as on-chip microthermometers were fabricated on the WSe_2 film. The distance between TM_{top} and TM_{bot} was set to 3 μm. The optical microscope images of each device are shown in Figure 2(b) (inset) and Figure 3(b).

Electrical measurements of the TAC-grown WSe_2 films were performed under ambient conditions using a Keithley 2612A source/meter unit. Thermoelectric power measurements of the TAC-grown WSe_2 films were also performed under ambient conditions using an Agilent B2912A precision source/meter unit and a Keithley 2612A source/meter unit (heating voltage source). The thermoelectric voltages were obtained by averaging 20 discrete points for each

varying heat voltage. The resistances of the microthermometer were obtained by averaging the values of varying heat voltages which were measured over 200 seconds.

Supporting Information
Supporting Information is available from the Wiley Online Library or from the author.

Acknowledgements
We gratefully acknowledge the generous support of the Science Foundation Ireland (SFI) for grants 12/RC/2278 and 15/IA/3131, the European Union Seventh Framework Program (Graphene Flagship, 604391), and National Research Foundation of Korea (NRF-2017M3A7B4049119).

References

[1] Radisavljevic, B., Radenovic, A., Brivio, J., Giacometti, V., Kis, A., *Nat. Nanotechnol.* **2011**, *147*, 6.

[2] Wang, Q. H., Kalantar-Zadeh, K., Kis, A., Coleman, J. N., Strano, M. S., *Nat. Nanotechnol.* **2012**, *699*, 7.

[3] Larentis, S., Fallahazad, B., Tutuc, E., *Appl. Phys. Lett.* **2012**, *223104*, 101.

[4] Das, S., Appenzeller, J., *Appl. Phys. Lett.* **2013**, *103501*, 103.

[5] Mak, K. F., Shan, J., *Nat. Photonics* **2016**, *216*, 10.

[6] Hu, Y., Huang, Y., Tan, C., Zhang, X., Lu, Q., Sindoro, M., Huang, X., Huang, W., Wang, L., Zhang, H., *Mater. Chem. Front.* **2017**, *24*, 1.

[7] Fleurial, J. P., Gailliard, L., Triboulet, R., Scherrer, H., Scherrer, S., *J. Phys. Chem. Solids* **1988**, *1237*, 49.

[8] Small, J. P., Shi, L., Kim, P., *Solid State Commun.* **2003**, *181*, 127.

[9] Small, J. P., Perez, K. M., Kim, P., *Phys. Rev. Lett.* **2003**, *256801*, 91.

[10] Shi, L., Li, D., Yu, C., Jang, W., Kim, D., Yao, Z., Kim, P., Majumdar, A., *J. Heat Transfer* **2003**, *881*, 125.

[11] Boukai, A. I., Bunimovich, Y., Tahir-Kheli, J., Yu, J.-K., Goddard Iii, W. A., Heath, J. R., *Nature* **2008**, *168*, 451.

[12] Zuev, Y. M., Chang, W., Kim, P., *Phys. Rev. Lett.* **2009**, *096807*, 102.

[13] Lee, C.-H., Yi, G.-C., Zuev, Y. M., Kim, P., *Appl. Phys. Lett.* **2009**, *022106*, 94.

[14] Hor, Y. S., Richardella, A., Roushan, P., Xia, Y., Checkelsky, J. G., Yazdani, A., Hasan, M. Z., Ong, N. P., Cava, R. J., *Physical Review B* **2009**, *195208*, 79.

[15] Xu, X., Gabor, N. M., Alden, J. S., van der Zande, A. M., McEuen, P. L., *Nano Lett.* **2010**, *562*, 10.

[16] Gabor, N. M., Song, J. C. W., Ma, Q., Nair, N. L., Taychatanapat, T., Watanabe, K., Taniguchi, T., Levitov, L. S., Jarillo-Herrero, P., *Science* **2011**, *648*, 334.

[17] Wu, P. M., Gooth, J., Zianni, X., Svensson, S. F., Gluschke, J. G., Dick, K. A., Thelander, C., Nielsch, K., Linke, H., *Nano Lett* **2013**, *4080*, 13.

[18] Kim, J., Lee, S., Brovman, Y. M., Kim, P., Lee, W., *Nanoscale* **2015**, *5053*, 7.

[19] Seol, J. H., Jo, I., Moore, A. L., Lindsay, L., Aitken, Z. H., Pettes, M. T., Li, X., Yao, Z., Huang, R., Broido, D., Mingo, N., Ruoff, R. S., Shi, L., *Science* **2010**, *213*, 328.

[20] Buscema, M., Barkelid, M., Zwiller, V., van der Zant, H. S., Steele, G. A., Castellanos-Gomez, A., *Nano Lett* **2013**, *358*, 13.

[21] Wu, J., Schmidt, H., Amara, K. K., Xu, X., Eda, G., Ozyilmaz, B., *Nano Lett* **2014**, *2730*, 14.

[22] Yoshida, M., Iizuka, T., Saito, Y., Onga, M., Suzuki, R., Zhang, Y., Iwasa, Y., Shimizu, S., *Nano Lett.* **2016**, *2061*, 16.

[23] Pu, J., Kanahashi, K., Cuong, N. T., Chen, C.-H., Li, L.-J., Okada, S., Ohta, H., Takenobu, T., *Phys. Rev. B* **2016**, 94.

[24] Lee, Y. H., Zhang, X. Q., Zhang, W., Chang, M. T., Lin, C. T., Chang, K. D., Yu, Y. C., Wang, J. T., Chang, C. S., Li, L. J., Lin, T. W., *Adv. Mater.* **2012**, *2320*, 24.

[25] Zhan, Y., Liu, Z., Najmaei, S., Ajayan, P. M., Lou, J., *Small* **2012**, *966*, 8.

[26] Lee, K., Gatensby, R., McEvoy, N., Hallam, T., Duesberg, G. S., *Adv. Mater.* **2013**, *6699*, 25.

[27] Huang, J.-K., Pu, J., Hsu, C.-L., Chiu, M.-H., Juang, Z.-Y., Chang, Y.-H., Chang, W.-H., Iwasa, Y., Takenobu, T., Li, L.-J., *ACS Nano* **2014**, *923*, 8.

[28] Yim, C., O'Brien, M., McEvoy, N., Riazimehr, S., Schäfer-Eberwein, H., Bablich, A., Pawar, R., Iannaccone, G., Downing, C., Fiori, G., Lemme, M. C., Duesberg, G. S., *Sci. Rep.* **2014**, *5458*, 4.

[29] Gatensby, R., McEvoy, N., Lee, K., Hallam, T., Berner, N. C., Rezvani, E., Winters, S., O'Brien, M., Duesberg, G. S., *Applied Surface Science* **2014**, *139*, 297.

[30] Huang, J., Yang, L., Liu, D., Chen, J., Fu, Q., Xiong, Y., Lin, F., Xiang, B., *Nanoscale* **2015**, *4193*, 7.

[31] Yim, C., Lee, K., McEvoy, N., O'Brien, M., Riazimehr, S., Berner, N. C., Cullen, C. P., Kotakoski, J., Meyer, J. C., Lemme, M. C., Duesberg, G. S., *ACS Nano* **2016**, *9550*, 10.

[32] Gatensby, R., Hallam, T., Lee, K., McEvoy, N., Duesberg, G. S., *Solid-State Electron.* **2016**, *39*, 125.

[33] Fang, H., Chuang, S., Chang, T. C., Takei, K., Takahashi, T., Javey, A., *Nano Lett* **2012**, *3788*, 12.

[34] Chuang, H. J., Tan, X., Ghimire, N. J., Perera, M. M., Chamlagain, B., Cheng, M. M., Yan, J., Mandrus, D., Tomanek, D., Zhou, Z., *Nano Lett* **2014**, *3594*, 14.

[35] Allain, A., Kis, A., *ACS Nano* **2014**, *7180*, 8.

[36] Liu, B., Ma, Y., Zhang, A., Chen, L., Abbas, A. N., Liu, Y., Shen, C., Wan, H., Zhou, C., *ACS Nano* **2016**, *5153*, 10.

[37] Imai, H., Shimakawa, Y., Kubo, Y., *Physical Review B* **2001**, 64.

[38] Chiritescu, C., Cahill, D. G., Nguyen, N., Johnson, D., Bodapati, A., Keblinski, P., Zschack, P., *Science* **2007**, *351*, 315.

[39] Tromp, R., Rubloff, G. W., Balk, P., LeGoues, F. K., van Loenen, E. J., *Phys. Rev. Lett.* **1985**, *2332*, 55.

[40] Slater, J. C., *The Journal of Chemical Physics* **1964**, *3199*, 41.

[41] Cordero, B., Gomez, V., Platero-Prats, A. E., Reves, M., Echeverria, J., Cremades, E., Barragan, F., Alvarez, S., *Dalton Trans* **2008**, *2832*.

[42] Schutte, W. J., De Boer, J. L., Jellinek, F., *Journal of Solid State Chemistry* **1987**, *207*, 70.

[43] Tonndorf, P., Schmidt, R., Böttger, P., Zhang, X., Börner, J., Liebig, A., Albrecht, M., Kloc, C., Gordan, O., Zahn, D. R. T., Michaelis de Vasconcellos, S., Bratschitsch, R., *Optics Express* **2013**, *4908*, 21.

[44] Zeng, H., Liu, G.-B., Dai, J., Yan, Y., Zhu, B., He, R., Xie, L., Xu, S., Chen, X., Yao, W., Cui, X., *Sci. Rep.* **2013**, *1608*, 3.

[45] Stanford, M. G., Pudasaini, P. R., Belianinov, A., Cross, N., Noh, J. H., Koehler, M. R., Mandrus, D. G., Duscher, G., Rondinone, A. J., Ivanov, I. N., Ward, T. Z., Rack, P. D., *Sci. Rep.* **2016**, *27276*, 6.

[46] Van Mieghem, P., *Rev. Mod. Phys.* **1992**, *755*, 64.

[47] Akdim, B., Pachter, R., Mou, S., *Nanotechnology* **2016**, *185701*, 27.

[48] Hippalgaonkar, K., Wang, Y., Ye, Y., Qiu, D. Y., Zhu, H., Wang, Y., Moore, J., Louie, S. G., Zhang, X., *Phys. Rev. B* **2017**, *115407*, 95.

[49] Cutler, M., Mott, N. F., *Phys. Rev.* **1969**, *1336*, 181.

[50] Fritzsche, H., *Solid State Commun.* **1971**, *1813*, 9.

[51] Muratore, C., Varshney, V., Gengler, J. J., Hu, J., Bultman, J. E., Roy, A. K., Farmer, B. L., Voevodin, A. A., *Phys. Chem. Chem. Phys.* **2014**, *1008*, 16.

[52] Taube, A., Judek, J., Lapinska, A., Zdrojek, M., *ACS Appl. Mater. Interfaces* **2015**, *5061*, 7.

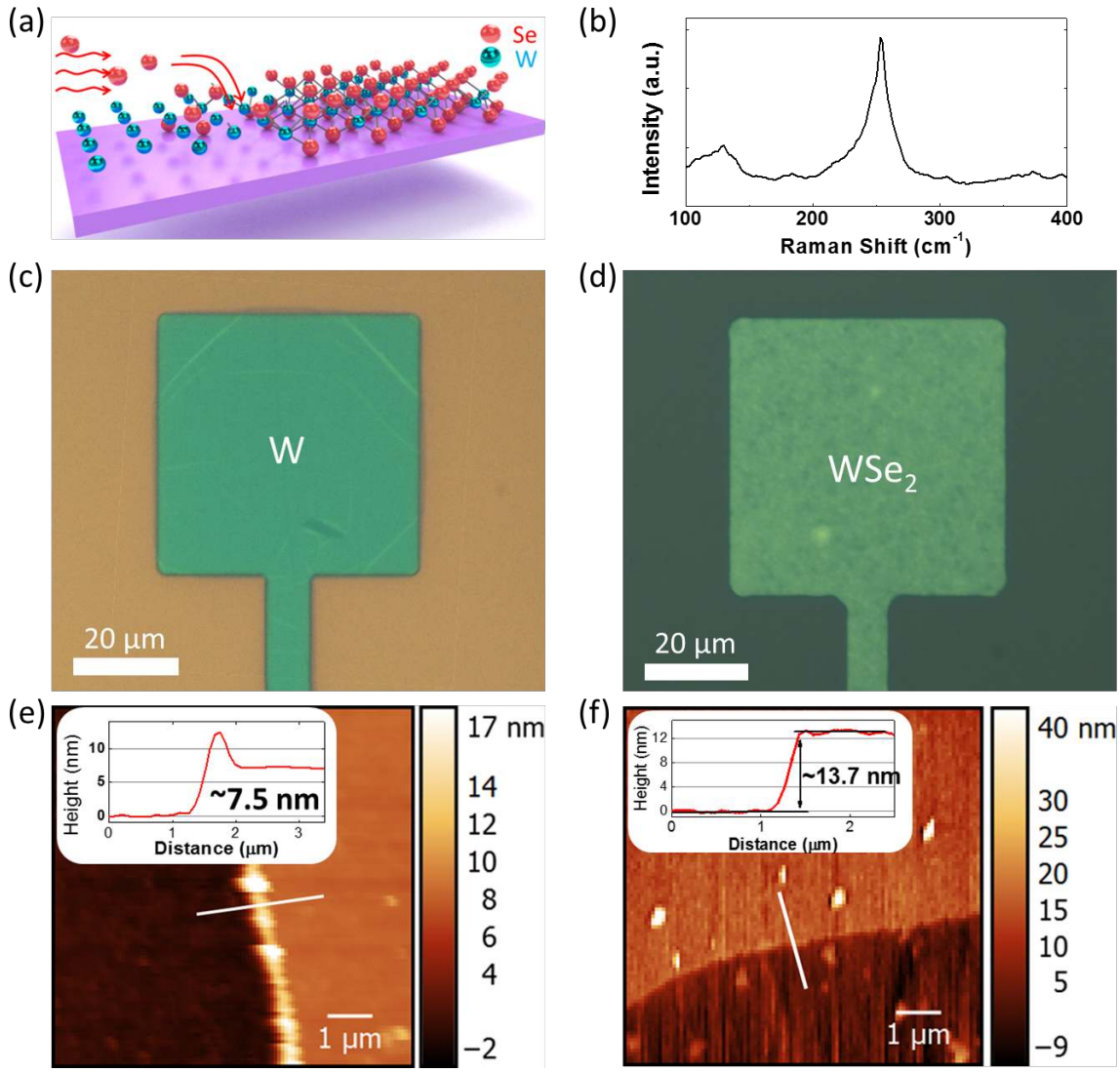

Figure 1. Synthesis and characterization of WSe_2 films. (a) Schematic image of TAC process for the conversion of W films to WSe_2. (b) Raman spectrum of TAC-grown WSe_2 films. (c) Optical microscope image of pre-defined structures of W film on SiO_2 and (d) TAC-grown WSe_2 film. Scale bar, 20 μm. (e) Atomic force microscopy (AFM) image of W film and (f) WSe_2 film. Insets: Height profile indicating the thickness of W film and TAC-grown WSe_2 film in Figure 1(e) and Figure 1(f).

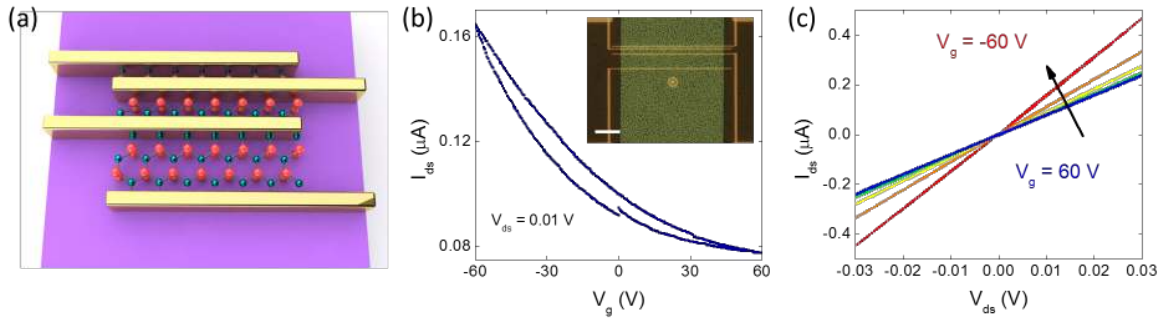

Figure 2. Electrical properties of TAC-grown WSe_2 thin films. (a) Schematic image of the WSe_2 devices with different channel lengths. (b) Transfer curve of WSe_2 FETs using the

substrate as a back gate. Inset: Optical microscope image of the WSe_2 device. (Scale bar = 20 μm) (c) Output characteristics of the WSe_2 FET using the substrate as backgate.

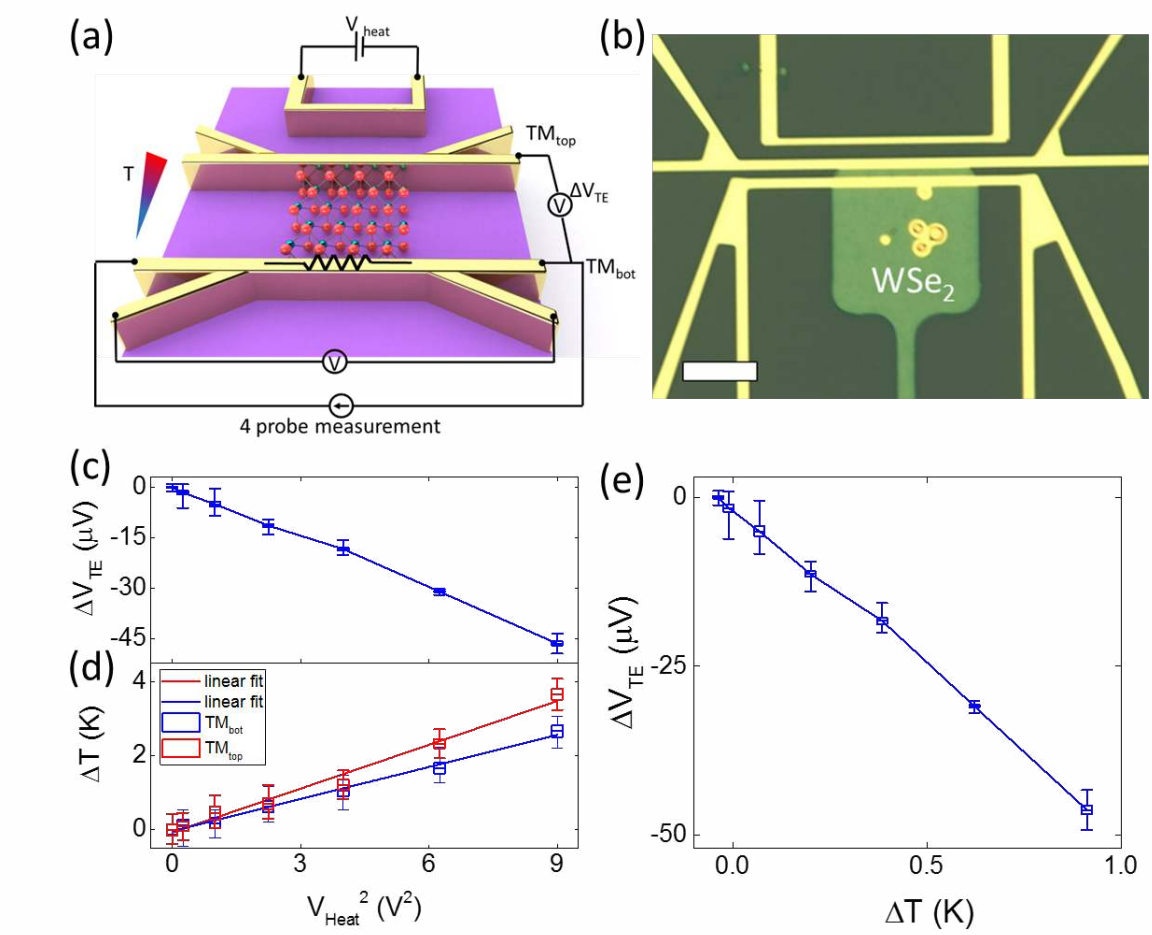

Figure 3. Thermoelectric power of WSe_2 films. (a) Schematic image of thermoelectric power measurement device. (b) Optical microscope image of the device (Scale bar, 20 μm). (c) Thermoelectric voltage (ΔV_{TE}) and (d) temperature gradient (ΔT) as a function of V_{heat}^2. (e) Relationship between ΔV and ΔT measured at $V_g = 0$ V.

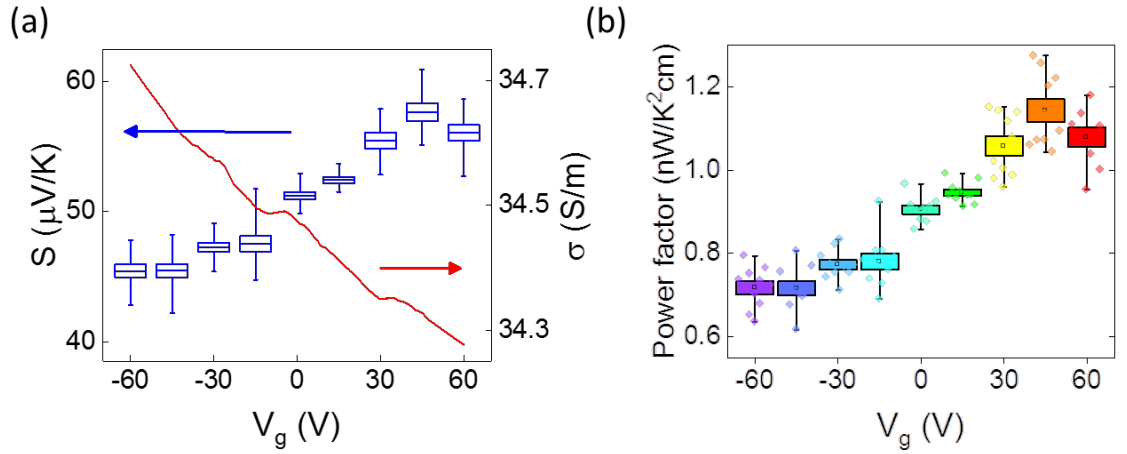

Figure 4. (a) The gate-voltage dependent electrical conductivity (σ, right y axis) and Seebeck coefficient (S, left y axis). (b) The gate-voltage dependent power factor ($S^2 \cdot \sigma$) of WSe_2 channels at room temperature under ambient conditions.

Table 1. Literature values for Seebeck coefficient for various nanomaterials.

Material	Preparation Method	Polarity	Maximum S ($\lvert S \rvert$, $\mu V\ K^{-1}$)	Reference
WSe_2	Mechanical exfoliation	Ambipolar	300	42
WSe_2	CVD	Ambipolar	350	26
Graphene	Mechanical exfoliation	Ambipolar	5–100	11, 28, 39
Bi_2Te_3	CVD	Ambipolar	250	9
Bi_2Se_3	CVD	Ambipolar	190	15
Carbon nanotube	CVD	Ambipolar	50	29–31
Bi nanowire	On film formation of nanowires	n-type	80	19
WSe_2	**TAC**	**p-type**	**61**	**This paper**